A&A manuscript no.
(will be inserted by hand later)

Your thesaurus codes are:
08(08.03.5; 13.25.5; 03.13.2)

ASTRONOMY
AND
ASTROPHYSICS
10.7.1995

Loop Modeling of Coronal X-ray Spectra

II. Parameter Constraints and Diagnostics

A. Maggio and G. Peres

Istituto ed Osservatorio Astronomico, Palazzo dei Normanni, I-90134, Palermo
E-mail: amaggio@oapa.astropa.unipa.it, gperes@oapa.astropa.unipa.it

Received December 5, 1994 / Accepted June 30, 1995

Abstract. We have investigated some aspects of the fitting of stellar X-ray spectra by means of hydrostatic models of coronal loops. We have performed an extensive set of simulations in which we have synthesized and fitted loop model spectra, considering the instrument responses of the *Einstein Observatory* Imaging Proportional Counter, of the *ROSAT* Position Sensitive Proportional Counter, and of the *ASCA* Solid-state Imaging Spectrometer, and we have derived theoretical confidence regions for the determination of the input loop parameters. We have found that our ability to constrain the loop model parameters depends on the distribution of the differential emission measure. More specifically, we have found that, for loops significantly below the pressure scale height, the spectral fitting allows to constrain well the plasma peak temperature and hence the product of the base pressure with the loop semi-length, but not each of the two separately, due to scale invariance of the equations describing the hydrostatic loop model of uniform pressure. For input loops with lengths of the order of the pressure scale height or larger, the spectral fitting yields closed confidence regions in the parameter space, allowing to constrain all the loop parameters, with different levels of discrimination depending on photon counting statistics and instrument energy response. Loops much longer than the star's radius and with relatively high base pressure behave like the short loops, because the pressure decrease along the loop is moderated by the local increase of the pressure scale height.

Key words: Stars:coronae; X-rays: stars; Methods: data analysis

Send offprint requests to: A. Maggio

1. Introduction

The analysis of X-ray spectra of late-type stars obtained with moderate, or medium energy resolution instruments, has typically shown good evidence of thermal emission and, therefore, the presence of coronae around these stars (see Rosner et al. 1985, for a review). The traditional conceptual tool, especially when analyzing spectra obtained with the *Einstein Observatory* Imaging Proportional Counter (IPC) (Gorenstein et al. 1981; Harnden et al. 1984) or the *ROSAT* Position Sensitive Proportional Counter (PSPC) (Pfeffermann et al. 1986), has been, so far, the description of the whole corona with one or two isothermal components (just to cite few recent works see Schmitt et al. 1990; Ottmann et al. 1993; Kashyap et al. 1994; Maggio, Sciortino & Harnden 1994). On the other hand, the analogy with the solar corona naturally leads one to assume the presence of closed coronal structures (loops) magnetically confining the plasma with different conditions and thermal stratification inside each loop, and entirely forming the X-ray emitting stellar corona.

In the analysis of *Einstein Observatory* IPC observations, the approach with one or two isothermal components was largely justified by the coarse spectral resolution. In the light of the better spectral resolution and sensitivity now available with *ROSAT* , and even more with *ASCA* , it is worth to start considering a more appropriate model in terms of an ensemble of coronal loops. The coronal loop scenario is certainly more realistic than the single- or double- isothermal plasma components, as the solar observations clearly show and physical intuition strongly suggests. At the price of a slightly more complex approach, loop modeling also offers a significantly deeper insight of the temperature and density stratification present in the corona.

Previous coronal loop modeling was largely developed for the solar corona. There is an extensive literature on detailed solar loop observations, mostly stemming from the X-ray observation program at AS&E led by the late

G. Vaiana, and matured with the Skylab S-054 X-ray experiment (for a review cf. Vaiana and Rosner 1978). The effort to model the observed coronal structures led to hydrostatic models of loops (Rosner, Tucker & Vaiana 1978, hereafter RTV; Serio et al. 1981) which were later proven to comply rather accurately with Skylab X-ray and UV observations (Pallavicini et al. 1981). An evolution of these models, adapted to describe loops in the coronae of late type stars, has been used in Ciaravella et al. (1994; henceforth Paper I), and in the present work.

An older version of our code was used by Schmitt et al. (1985) to fit *Einstein Observatory* IPC observations of Procyon, and by Giampapa et al. (1985) to fit observations of several active stars. We shall comment some of these earlier results in the light of our findings.

Other attempts of spectral fitting with loop models were performed by Stern et al. (1986) on IPC X-ray spectra of four dwarfs in the Hyades cluster, by Schrijver et al. (1989) on the spectra of the active binaries Capella and σ^2 CrB observed with the EXOSAT Transmission Grating Spectrometer, and more recently by Ottmann et al. (1993) and Ottmann (1993) on the X-ray emission of the RS CVn-like system AR Lac observed with the *ROSAT* PSPC. All these works were based on the loop model of Vesecky et al. (1979), which incorporates the effect of variable loop cross section. Good fits to the observed spectra were usually obtained with small expansion area factors (≤ 2), except in the case of Capella and σ^2 CrB where a two-loop model fitting was performed, and expansion factors larger than about 5 were derived.

This work is the second in a series dedicated to clarify some aspects of coronal loop physics and to interpret stellar coronal emission in terms of loops emission. Paper I has addressed some aspects important for the following steps. It has shown that departures from Spitzer conductivity, although important for a physically correct model of the plasma in some loops, are marginally relevant, if at all, for the analysis of realistic coronal spectra. It has also shown that the expansion of the loop's cross section could sometimes influence the spectrum emitted by loops, but its effect may be marginal. Furthermore and most important, especially for the present work, the loop spectrum differs radically from that of an isothermal plasma of the same effective temperature, with differences probably observable already with currently available instruments. It appears that interpreting spectra in terms of isothermal components can be misleading if one wants to derive the characteristics of the loops present on the star and that, to this end, one should try to fit the stellar emission directly in terms of loops emission.

In this paper we therefore investigate the diagnostic power of the loop model, and the constraints on loop model parameters we can obtain from the analysis of stellar X-ray spectra, depending on the spectral resolution of the detector and on photon counting statistics. We have considered three instruments already flown: the *Einstein Observatory* IPC, the PSPC on board the *ROSAT* satellite, and the Solid-state Imaging Spectrometer (SIS) operating on the *ASCA* mission (Tanaka et al. 1994).

In Sect. 2 we describe the hydrostatic loop model, and in Sect. 3 we illustrate the simulations performed. Our results are described in Sect. 4 and discussed in Sect. 5. Finally, Sect. 6 is devoted to a summary and to our conclusions.

2. The Loop Model

As for the non-varying stellar coronal emission, one can assume that most of the emission originates from loops which change little (if at all) over the characteristic cooling time of the plasma. In order to study such an emission we have used a new version of the well tested Serio et al. (1981) hydrostatic model of coronal loops, in which the distributions of plasma temperature and density along the field lines are computed by solving the equations of steady energy balance, of hydrostatic equilibrium, and of state. We have assumed radiative losses due to an optically thin plasma with cosmic abundances, according to the model by Raymond & Smith (1977), and the classic Spitzer (1962) thermal conduction, in the light of the results of Paper I. Given the effectiveness of conduction in redistributing heat in the corona we have assumed a uniform heating along the loop; as we show in Sect. 5.3, this assumption has little effect on the results (Withbroe 1981; see also Peres, Reale & Golub 1994).

Our loop model is completely determined by any two parameters, selected among the following: the pressure at the base of the transition region, p_0, the loop semilength, L, the maximum temperature (at the top), $T_{\rm max}$, or the heating per unit volume, $E_{\rm H}$. All these quantities are linked by the following scaling laws, here adapted from Serio et al. (1981):

$$T_{\rm max} \approx 1.4 \times 10^3 (p_0 L)^{1/3} \exp(-0.04 L/s_{\rm p}) \qquad (1)$$

$$E_{\rm H} \approx 10^5 p_0^{7/6} L^{-5/6} \exp(-0.5 L/s_{\rm p}) \qquad (2)$$

where $s_{\rm p} = 2kT/\mu m_{\rm H} g_* \sim 5 \times 10^3 T g_\odot / g_*$ is the pressure scale height, evaluated at the loop apex. Note that the exponential factor is important only for loops rising significantly above the pressure scale height; for smaller loops the scaling laws reduce to the simpler form derived by RTV.

The above scaling laws were derived and tested for loops shorter than a stellar radius; for very long loops, the r^{-2} functional form of gravity can have a significant effect. In fact, integrating the hydrostatic balance equation, the pressure follows the general law

$$p = p_0 \exp\left(-\frac{\mu m_{\rm H}}{2k} \int_{r_0}^{r} \frac{g(s) {\rm d}s}{T(s)}\right) \qquad (3)$$

where $g(s)$ and $T(s)$ are, respectively, the gravity component and the plasma temperature and s, the field line coordinate along the loop. Therefore, pressure does not necessarily fall exponentially, but for long loops it might tend to an asymptotic value. This topic will be important when discussing our results.

As in Paper I, we have assumed a different loop geometry with respect to previous works, namely a circular arch of constant cross section anchored on the *spherical* stellar surface, rather than on a plane surface. We refer to Paper I for more details.

From the distributions of temperature and density provided by the model, we have computed the optically-thin spectrum emitted by the whole loop, using the Raymond-Smith emissivity code for a plasma in thermal equilibrium (Raymond & Smith 1977; Raymond 1989). Whenever needed, this spectrum has been convolved with the effective area and energy response matrix of the selected instrument (see Sect. 3.3) in order to obtain a synthesized spectrum in detector energy bins, realistically simulating an observation. These computations have been performed using the Analysis System for Astrophysical Plasmas (ASAP; Maggio et al. 1994).

3. Simulations

Our approach has been to synthesize the spectra of stellar coronae whose emission is dominated by a single class of loops, and then to perform a spectral fitting over a grid of loop models, to evaluate the statistical confidence regions for the determination of the input loop parameters. In other words, the aim has been to test our ability to recover the input loop parameters through the fitting. In this way, we test the sensitivity of the fitting results both to the specific input loop parameters and to the observing instrument.

3.1. Parameter Space and Grid Models

We model the coronal structures on one star in the middle of the class of late-type dwarfs, namely a G0 V star with radius of 7.3×10^{10} cm and surface gravity of 2.7×10^4 cm sec^{-2}.

The range of parameters used for our simulations was chosen to cover a large set of conditions possibly found in a non-flaring solar-type corona. In particular, we have computed a set of 50×20 loop models (hereafter called *grid models*) in the $p_0 - L$ parameter space, spanning at equal steps in the logarithm the ranges $\log\, p_0\, (\mathrm{dyne\ cm^{-2}}) = [-0.5, 1.95]$ and $\log\, L\, (\mathrm{cm}) = [8.5, 13.25]$. The corresponding range of peak temperatures explored was $\log\, T_{\max}\, (\mathrm{K}) \approx [5.8,8.2]$. This choice also allows us to explore the characteristics of loops ranging from those so short that plasma pressure is nearly uniform, to those with a sizable pressure decrease, and finally, to very long ones.

Note that, for the longest loops here considered, the sound crossing time

$$\tau \sim \frac{L}{c_s} = 66.7\, \frac{L_9}{T_6^{1/2}} \qquad (4)$$

where c_s is the sound speed, L_9 and T_6 are the semi-length and the peak temperature in units of 10^9 cm and 10^6 K, respectively, can amount to $\sim 10^5$ sec. Even in such extreme cases the hydrostatic hypothesis could be taken as valid anyhow, if observations show no variability over such a time scale. We refer to Sect. 5 for a more detailed discussion and warning on the longest loops.

3.2. Input Models

We have performed an extensive set of simulations by assuming different input loop models within the chosen parameter space (not necessarily coincident with any of the grid models).

In the following, we focus our attention on the simulations made with twelve loop models (hereafter called *input loops*), listed in Tab. 1, which describe the different characteristics of the spectral fitting solutions we have found on a significantly larger set of cases. Since we have verified that the results differ for loops with vertical extents, H, either larger or smaller than the pressure scale height, s_p, the twelve input loops have been selected by combining four values of the loop base pressure, $p_0 = 2, 5, 10, 25$ dyne cm^{-2}, with three values of $H/s_p \approx 0.2$, 1, and 5. [1]

We stress that while we keep using in the following the parameter H/s_p because of its intuitive meaning, the pressure scale height may not be formally defined for loops extending much higher than the stellar radius (see Sect. 2). In fact, for such loops the pressure may never drop to $1/e$ of its value at the base, in spite $H \gg s_p$. In order to explore a wide range of cases, we have considered also loops with very large vertical extents ($L \sim 10^{12}$ cm): in spite of the fact that these are very extreme and perhaps unrealistic cases, they are fundamental to clarify the competing role played by the loop length with the star's gravity in determining the amount of high-temperature emitting plasma near the loop apex (see Sect. 5). We anticipate that this interplay is what *really* establishes the shape of the X-ray spectrum, while the quantity H/s_p may not be significant.

3.3. Observing Instruments

The three X-ray detectors here considered are the *Einstein Observatory* IPC, the *ROSAT* PSPC, and the *ASCA* SIS, used at the foci of grazing incidence X-ray telescopes with different collecting area. We note that the first two

[1] In practice, from any combination of p_0 and H/s_p we have iterated to find the value of the semi-length, L (see Tab. 1), appropriate for the loop solution.

Table 1. Input Loop Parameters

Ref.	p_0 (dyne cm^{-2})	L (cm)	$T_{\rm max}$ (10^6 K)	$T_{\rm eff}^{\rm IPC}$ (10^6 K)	$T_{\rm eff}^{\rm PSPC}$ (10^6 K)	$T_{\rm eff}^{\rm SIS}$ (10^6 K)	$H/s_{\rm p}$
a	2	5.8×10^{9}	3.2	2.3	2.2	2.7	0.2
b	5	9.1×10^{9}	5.0	3.7	3.5	4.2	0.2
c	10	1.3×10^{10}	7.2	5.2	5.0	5.7	0.2
d	25	2.0×10^{10}	11.3	7.2	7.1	8.0	0.2
e	2	7.8×10^{10}	7.4	4.4	4.1	5.2	1.0
f	5	1.2×10^{10}	11.6	6.3	6.1	7.3	1.0
g	10	1.7×10^{10}	16.4	8.1	7.7	9.0	0.9
h	25	2.8×10^{11}	25.7	11.7	10.7	25.8	1.0
i	2	6.7×10^{11}	13.9	5.1	4.8	6.5	5.1
j	5	1.1×10^{12}	22.0	7.9	7.2	9.0	5.2
k	10	1.5×10^{12}	31.1	11.6	10.2	12.3	5.3
m	25	2.4×10^{12}	49.1	20.7	17.5	20.2	5.4

are proportional counters, and the third is a CCD detector. Among other characteristics, the most relevant for our work are the energy band and the spectral resolution, $\Delta E/E$: the *Einstein Observatory* IPC is sensitive to X-rays in the range 0.16-4 keV, with $\Delta E/E \sim 1$ at 1 keV; the *ROSAT* PSPC is characterized by a softer energy band, 0.1-2.4 keV, and better spectral resolution, $\Delta E/E \sim 0.4$ at 1 keV; finally, the *ASCA* SIS has a wider but harder energy band, 0.5-10 keV, and $\Delta E/E$ between 0.06 and 0.1 at 1 keV, depending on the read-out noise.

The energy response of these instruments is satisfactorily described for our purposes by (i) the effective area curve and (ii) the energy redistribution matrix (or briefly, response matrix). The latter describes the probability that an input photon of a given energy is detected in any of pre-defined energy bins ("channels"): the *Einstein Observatory* IPC spectra are binned in 15 channels, while 34 channels are usually employed for the *ROSAT* PSPC, and 512 channels for the *ASCA* SIS.

An important feature of these instruments is their sensitivity, as expressed by their effective area; however, here we do not deal with the detectability of X-ray sources, since we have studied sources with a fixed total number of counts (see the next section). This issue was addressed to some extent in Paper I.

For all the grid models we have computed the instrument-folded effective temperature, $T_{\rm eff}$, a quantity useful for comparison with the typical temperatures obtained by fitting real spectra. This is defined as

$$T_{\rm eff} = \frac{\int T(s)\, n_{\rm e}(s)\, n_{\rm H}(s)\, G(T(s))\, {\rm d}V}{\int n_{\rm e}(s)\, n_{\rm H}(s)\, G(T(s))\, {\rm d}V} \tag{5}$$

where $T(s)$ is the plasma temperature distribution vs. the coordinate, s, along the loop, $n_{\rm e}$ and $n_{\rm H}$ are the plasma electron and hydrogen densities, and $G(T)$ is the instrument-folded plasma emissivity:

$$G(T) = \int P(T,E) A(E) {\rm d}E \tag{6}$$

being $P(T,E)$ the radiative function per unit emission measure for an optically-thin plasma in thermal equilibrium, and $A(E)$ the instrument effective area vs. energy, E. The interpretation of $T_{\rm eff}$ is that of an average plasma temperature weighted by the emission measure distribution, the plasma radiative function and the instrument response (see Paper I). This quantity is more appropriate than the loop peak temperature as an estimate of the temperature which can be derived from the fitting of observed spectra with isothermal models. In Fig. 1 we show contour levels of $T_{\rm max}$ and $T_{\rm eff}$ over the assumed $p_0 - L$ parameter space for the *Einstein Observatory* IPC, and in Tab. 1 we have reported the values of $T_{\rm eff}$ for the selected input loops. It is worth noting that, since the instrumental characteristics enter in the definition of $T_{\rm eff}$, the latter are slightly different for different instruments (see Tab. 1), even for the same loop model.

3.4. Model Spectra

We have performed simulations for each of the above input loops and each of the instruments, and we have synthesized the parent loop spectrum, including absorption due to an hydrogen column density $N_{\rm H} = 10^{19}\ cm^{-2}$ in the interstellar medium (typical of nearby stars), as follows:

$$C(j) = \int \int n_{\rm e}\, n_{\rm H}\, {\rm e}^{-\sigma(E) N_{\rm H}} \times$$

$$\times \frac{P(T,E)}{E} A(E)\, R(j,E)\, {\rm d}E\, {\rm d}V \tag{7}$$

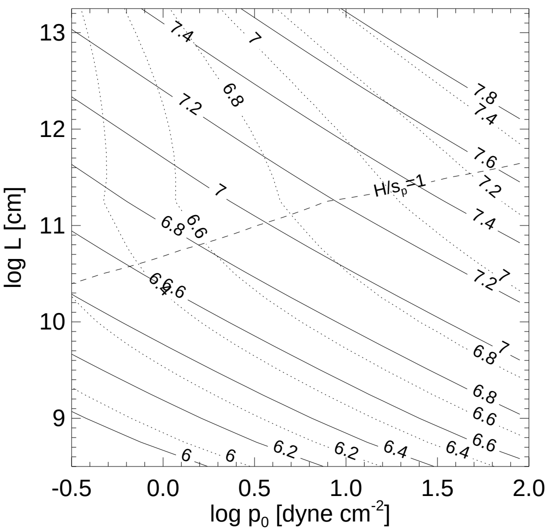

Fig. 1. Contour levels of the maximum loop plasma temperature, $T_{\rm max}$ (solid lines), and of the effective temperature (see text), $T_{\rm eff}$ (dotted lines), over the $p_0 - L$ parameter space explored. The effective temperatures are derived assuming observations with the *Einstein Observatory* IPC. The labels along the lines indicate the values of log T (K). The slanted dashed line marks the locus where the loop height, H, is equal to the pressure scale height at the loop apex, $s_{\rm p}$. Note that the iso-$T_{\rm max}$ and iso-$T_{\rm eff}$ lines are nearly parallel for loops with height significantly below the pressure scale height.

where $C(j)$ is the count rate in the j-th instrument channel, $\sigma(E)$ is the photoelectric cross-section per hydrogen atom for absorption of photons of energy E by the interstellar medium (Morrison & McCammon 1983), $R(j, E)$ is the instrument response matrix, and all the other terms have been already defined above. This spectrum has been normalized to the desired total number of detected counts, in all the instrument channels later used for the fitting. In particular, we have considered two levels of counting statistics, namely 10^3 and 10^4 total detected counts, for the *Einstein* IPC and the *ROSAT* PSPC, and 10^4 total counts for the *ASCA* SIS.

Note that we have only imposed a realistic number of total counts and we have not considered explicitly the combination of stellar surface filling factor of the coronal loops, source distance, and exposure time needed to produce that number of observed counts. In fact, only the number of counts is really crucial for the points we want to make. However, in order to see how this corresponds to the characteristics of a real observation and to put our results in an appropriate frame, we note that if we assume complete filling of the star's surface and a distance of 10 pc, the exposure time required to collect 10^4 counts ranges from few hundreds seconds for the highest pressure loops when observed with *ROSAT* , to $\sim$ 10^5 sec for the loop with the lowest pressure and length when observed with *ASCA* .

The next step has been to generate 1000 realizations of the synthesized loop spectrum by adding Poisson noise, i.e. purely statistical noise, to the parent loop spectrum. No contamination by diffuse X-ray background has been taken into account because of the relatively high counting statistics assumed for the simulated sources.

The 1σ errors on the number of counts in each instrument channel, n_c, have been computed using the approximation $\delta(n_c) = 1 + (n_c + 0.75)^{1/2}$ for events obeying Poisson statistics (Gehrels 1986), instead of the less accurate Gaussian approximation.

3.5. χ^2 Fitting and Contour Levels in the Parameter Space

Each of the 1000 realizations can be considered as (i.e. simulates) a different observation of the same object: a corona with a dominating kind of loop. Under this assumption, with the following analysis we have tested how the various instruments are able to discriminate coronal loop spectra by a χ^2 fitting of the simulated spectra with model spectra of coronae of the same kind, chosen within a range of loop parameters.

For each of the 1000 spectrum realizations we have performed a search of the minimum χ^2 value over the grid of model spectra. The crucial difference between the simulated spectra and the grid model spectra is that the former include the proper statistical noise, while the latter are theoretical, noiseless spectra. The aim of the whole simulation is to accumulate a large number (1000) of spectral fitting results, i.e. "best-fit" theoretical models, which are distributed in the two-dimensional parameter space explored. The extent and shape of the region in the parameter space where the 1000 "best-fit" models fall, give us information on the statistical uncertainty associated with the best-fit model parameters which would be found with a similar analysis performed on a spectrum actually observed.

To quantify this uncertainty, at a given statistical confidence level, we have evaluated the contour levels in the parameter space, corresponding to the 68% and 90% quantiles of the cumulative distribution of the occurrences of "best-fit" models, as follows. First, we have generated the integral distribution of the number of occurrences for all the models in the search grid, i.e. the step-wise function

$$I(k) = \sum_{\{m_i\} \geq k} m_i \tag{8}$$

where m_i is the number of times that the i-th grid model turned out to be the "best-fit" model, and $I(k)$ therefore yields the total number of occurrences related to grid models found as "best-fit" models k times or more. Then, from the $I(K)$ value at the 68% and 90% of the total number of realizations, we have found the corresponding k (i.e., in our case, the value k at which $I(k) = 680$ or 900). Finally, we have drawn contour levels at these k values on the distribution of m_i in the parameter space. In this

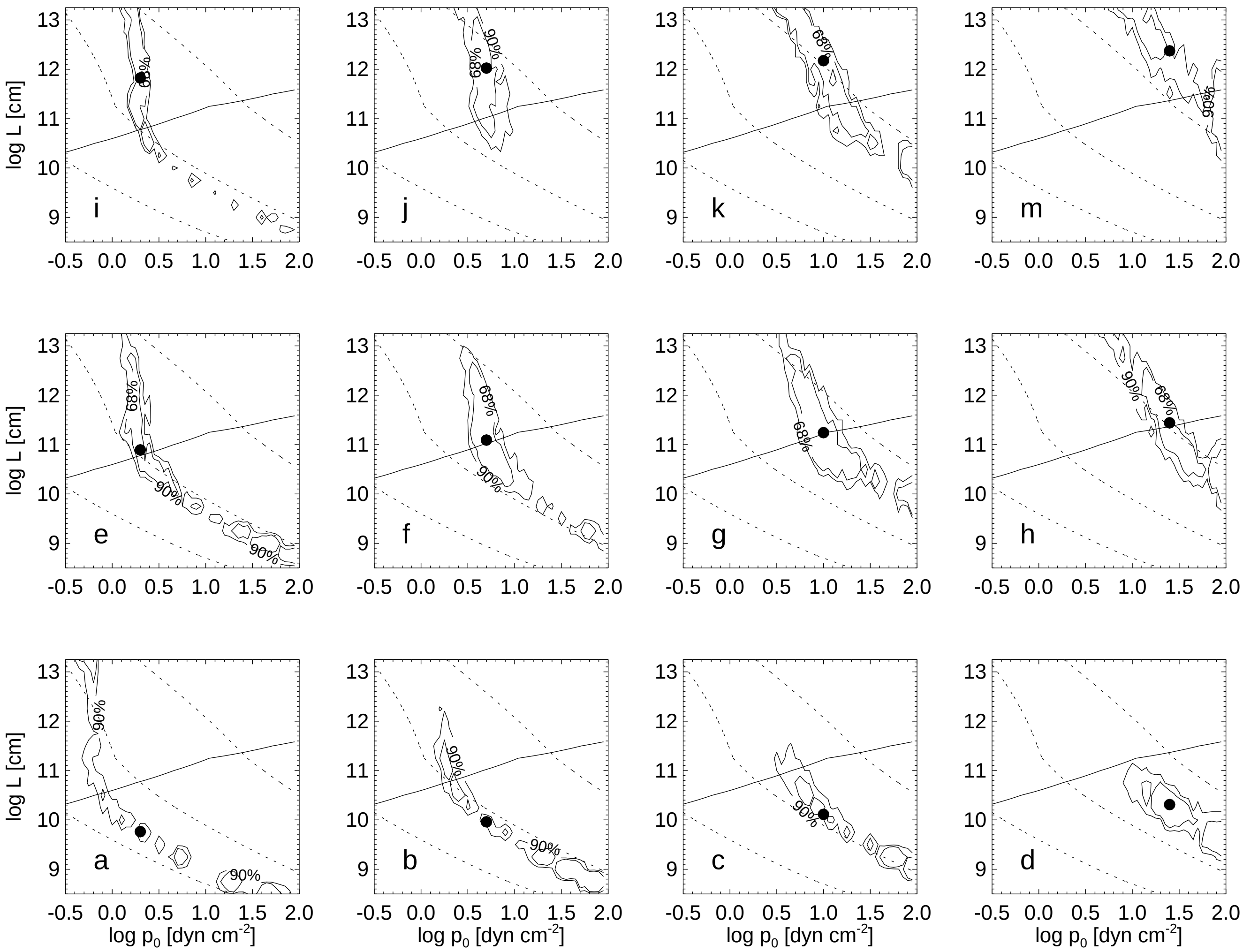

Fig. 2. Probability contour levels at 68% and 90% in the $p_0 - L$ parameter space, obtained from the simulations performed with the twelve input loops (see Table 1), and assuming that a spectrum with 10^3 counts has been collected with the *Einstein Observatory* IPC. In each panel, pertaining to a different simulation, the input loop is indicated by the filled circle. The twelve panels are arranged so that the input loop base pressure is the same for the panels in each column and it increases moving from the left to the right column, while the H/s_p ratio of the input loop is fixed along the rows and increases moving from bottom to top. The letters in the bottom-left corners can be used to identify the input loop characteristics in Table 1. The solid line marks the $H = s_p$ locus. The dotted lines are the contour levels of iso-$T_{\rm eff}$ corresponding to log $T_{\rm eff}$ (K) = 6.3, 6.7, and 7.1, moving from bottom left to top right of each panel.

way, the models in the inner contour, corresponding to the 68% level, are the "best-fit" models for this percentage of the total number of realizations, and this contour can be compared with the corresponding confidence level derived from the analysis of real data. The 90% contour can be compared in a similar fashion.

4. Results

4.1. Simulations of Einstein Observatory IPC spectra

In Fig. 2 we show the 68% and the 90% contour levels (as defined above) in the $p_0 - L$ parameter space, obtained from the simulations performed with the twelve input loops. In each panel, corresponding to a different fitting simulation, the input loop is marked by the filled circle. The fitted spectra contain in all cases 10^3 counts, apart statistical fluctuations.

These simulations indicate that in all cases there is an elongated, banana-shaped region (hereafter called "confidence" region) in the parameter space where the best-fit models are found (the presence of several "islands" within this region is due to the discreteness of the model grid on which the χ^2 search has been performed). This result indicates that, with the *Einstein*/IPC and the assumed number of counts in the spectrum, the loop model parameters can be constrained by the spectral fitting only

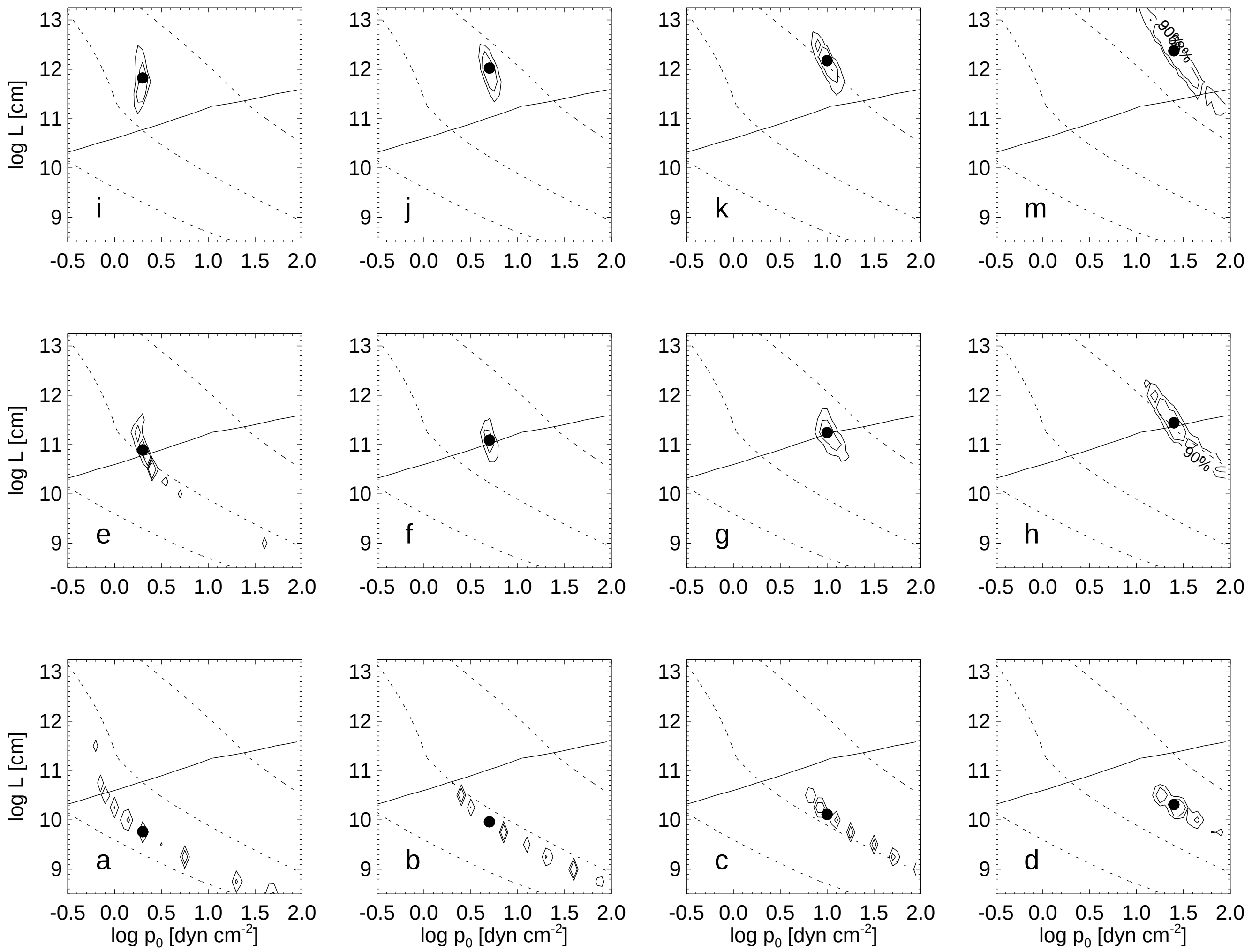

Fig. 3. Similar to figure 2 except that we have considered 10^4 counts in the input loop spectra. Note the improvement in the spectral fitting solutions due to the increased counting statistics.

along such elongated region. However, it is worth noting that the confidence region in the $p_0 - L$ parameter space is relatively narrow, it follows closely the lines of constant $T_{\rm eff}$ below the $H = s_{\rm p}$ line, and it tends to be slightly more vertical than the $T_{\rm eff}$ lines if it extends above such a line. Note also that many of these confidence regions do not appear closed at their extremes, i.e. they extend to high-L, low-p_0 regions and/or to low-L, high-p_0 regions, especially in this relatively low count rate case.

We can expect some improvement in our ability to recover the input loop parameters with the increase of the counting statistics, and this is confirmed by the simulations performed with an higher number of counts ($\sim 10^4$) (Fig. 3): for the input loops with $H < s_{\rm p}$ (cases a – d in Tab. 1) and for all the high-pressure ($p_0 = 25$ dyne cm^{-2}) loops (cases h and m) there is again an elongated confidence region where the best fit parameters can be found, which is narrower than in the previous case but still extended, while for the other input loops, namely those with $H \geq s_{\rm p}$ (mid and upper panel rows in the figure), this region is definitely more compact and better localized. Note also that, for the input loops below the pressure scale height, the confidence region usually rests below the $H = s_{\rm p}$ locus, while for the input loops with $H/s_{\rm p} > 1$ it is above that locus, with the only exceptions of the high pressure cases with $p_0 = 25$ dyne cm^{-2} (cases h and m).

4.2. Simulations of ROSAT PSPC spectra

Moving to the simulations of spectra observed with the *ROSAT* PSPC (Fig. 4 and 5), we have tested the improvement that the better spectral resolution of this instrument, with respect to the *Einstein* IPC, brings in our ability to constrain the loop model parameters. Comparing Fig. 4 with Fig. 2, we find that PSPC spectra with 10^3 counts yield relatively narrower elongated confidence regions, with respect to those obtained with IPC spec-

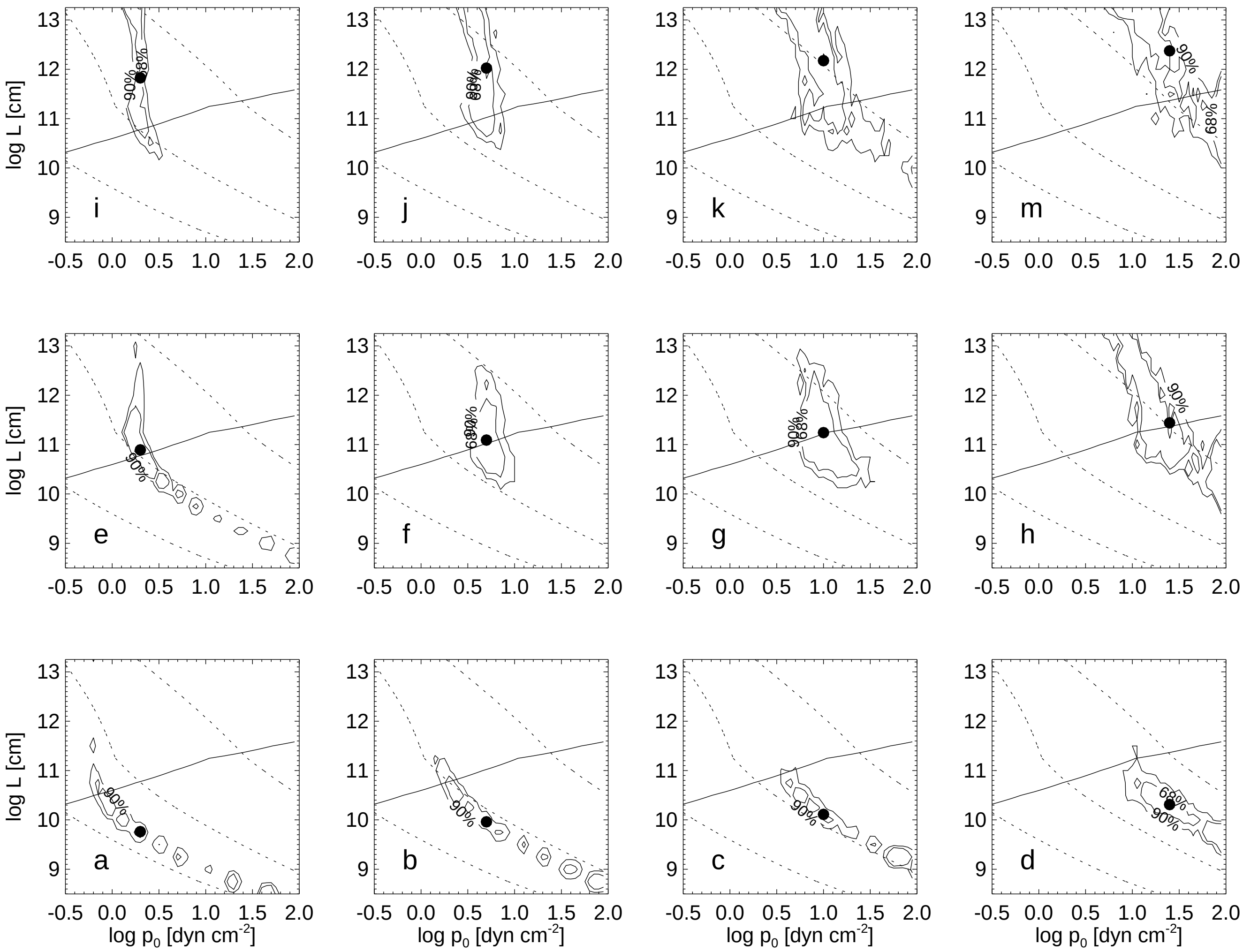

Fig. 4. Similar to figure 2 but assuming that a spectrum with 10^3 counts was collected with the *ROSAT* PSPC. The iso-$T_{\rm eff}$ lines are slightly different with respect to figure 2 and 3, because of the different spectral response of the instrument.

tra, in the case of input loops below the pressure scale height, more localized regions for the input loops f and g with $H/s_{\rm p} \sim 1$, and almost vertical regions for the low-pressure loops (cases i and j) above the $H = s_{\rm p}$ locus.

Increasing the number of counts in the PSPC spectra to 10^4 (Fig. 5), our simulations show that the solutions of the spectral fitting, in the case of input loops with $H \geq s_{\rm p}$ and $p_0 \leq 10$ dyne cm^{-2}, are densely clustered in a very limited, closed region of the parameter space surrounding the input parameter values. Note that, since in these cases the confidence region is narrow and almost vertical, the plasma base pressure is better constrained than before, while some residual uncertainty remains in the determination of the loop semi-length (and hence on the loop peak temperature). Instead, for input loops with $H < s_{\rm p}$, the loop effective temperature is the parameter best constrained, while the loop semi-length and base pressure cannot be separately determined: any model with a combination of p_0 and L such that $T_{\rm eff}$ remains fixed may yield an equally good fit of the input loop spectrum. Since, in this region of the parameter space, $T_{\rm max}$ is roughly proportional to $T_{\rm eff}$, also the peak temperature is well constrained.

4.3. Simulations with ASCA SIS spectra

Along the same trend traced above, we have found again different shapes of the confidence region depending on the input loop, also for the *ASCA* SIS spectra (Fig. 6): for input loops below the pressure scale height the confidence region is narrow, and extends along lines of constant effective (and peak) temperature, i.e. again $T_{\rm max}$ is well constrained but not p_0 and L separately; for input loops with $H \gtrsim s_{\rm p}$, all the loop parameters can be well constrained, and the input loop almost precisely recovered. Note that in the latter case, the residual uncertainty on the loop semi-length (or peak temperature) found with the analysis of PSPC spectra is now largely reduced. As discussed in

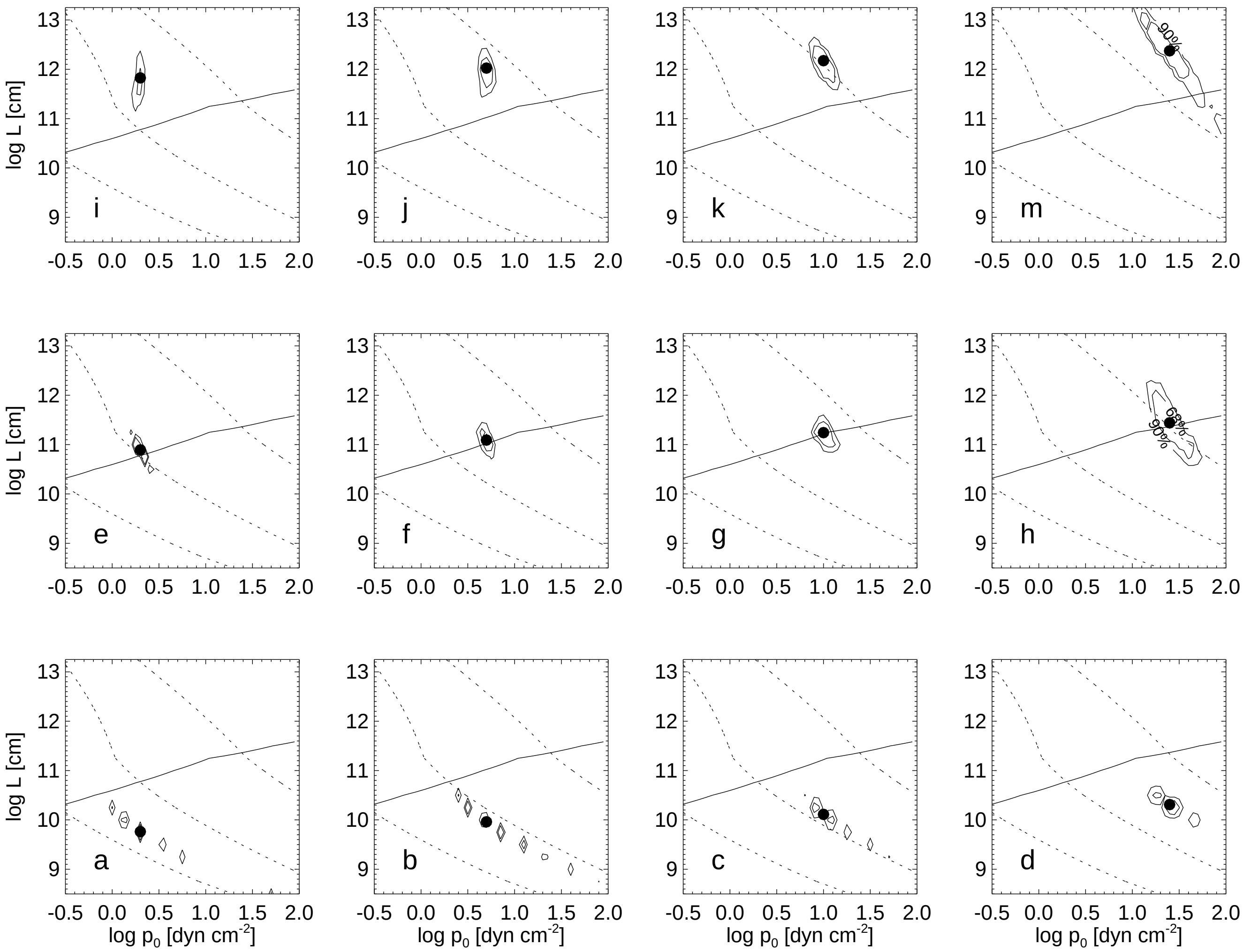

Fig. 5. Similar to figure 4, but assuming input loop spectra with 10^4 counts.

the following, this improvement is likely due to the wider energy band covered by the *ASCA* SIS.

5. Discussion

5.1. Characteristics of the simulation results

For convenience, we discuss separately the three general classes of solutions that we have recognized for (a) input loops below the pressure scale height, (b) loops as high as the pressure scale height or longer, and (c) high pressure loops.

(a) Input models with $H < s_p$

The spectral analysis yields open, banana-shaped confidence regions, comprising fitting models with almost constant plasma effective (and peak) temperature. Therefore, while p_0 and L, if taken separately, are undetermined, their product is well determined. The width of the confidence region decreases (i.e. $T_{\rm eff}$ and $T_{\rm max}$ are better constrained) with increasing number of counts in the spectrum, and resolving power of the instrument.

The characteristics of this class of models were already pointed out by Schmitt et al. (1985), who performed a loop model analysis of the X-ray emission of Procyon, and attributed them to the link among $T_{\rm max}$, p_0 and L through the RTV scaling law (see also Serio 1985). This law, valid only for loops below the pressure scale height, implies that the same top temperature can be achieved by different combinations of base pressure and semi-length.

The equivalence of the models having virtually constant pressure and the same $T_{\rm max}$ is based on a more fundamental characteristic: the shape of the emission measure distribution is completely determined by the product $p_0 L$, and so is the emitted spectrum, apart from a normalization factor. In stellar observations, the latter would be indistinguishable from an area coverage factor. We note that this result was already implicit in the analytic expression of the temperature variation along the loop and of the differential emission measure presented by Rosner

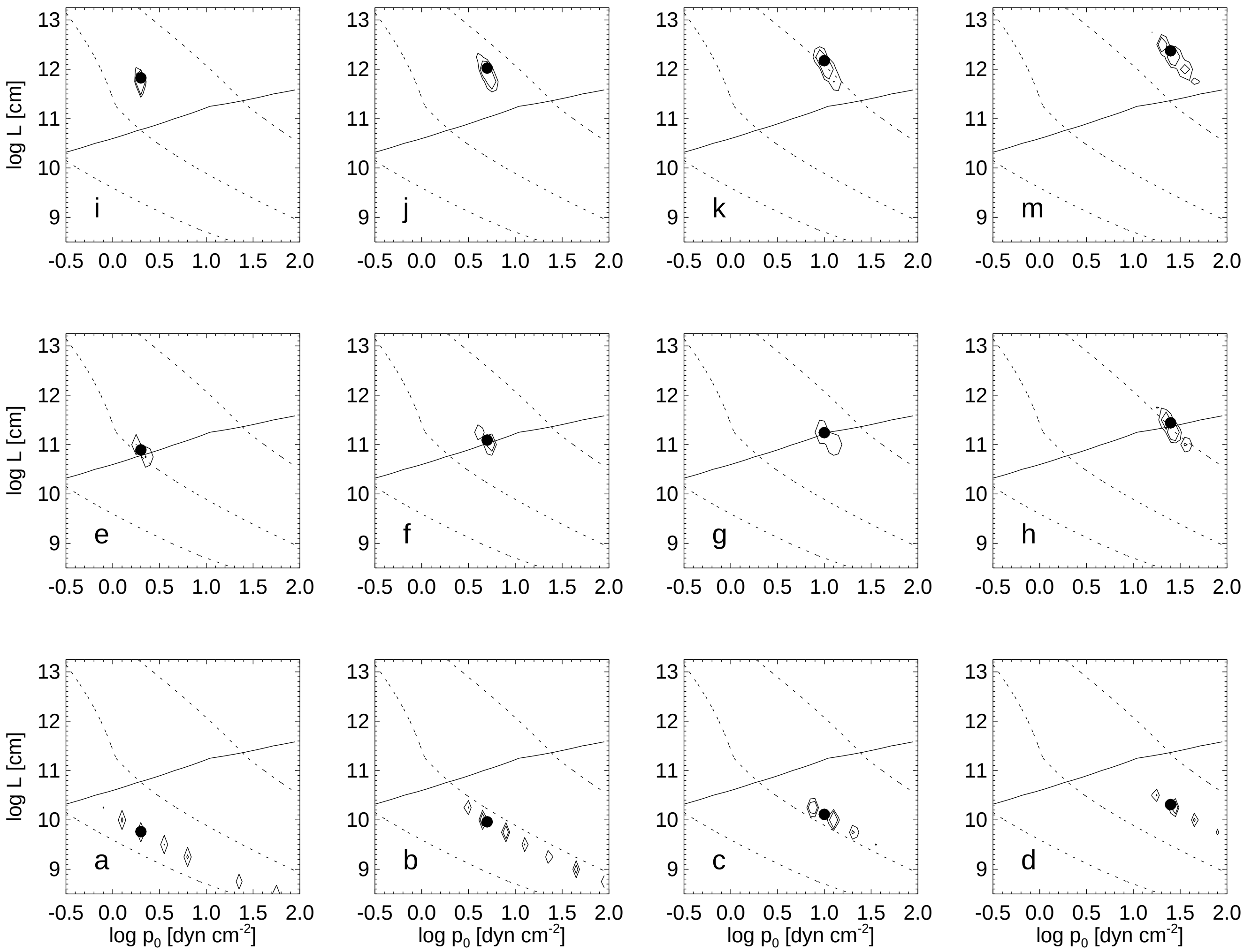

Fig. 6. Similar to figure 3 and 5, but assuming input loop spectra with 10^4 counts observed with the *ASCA* SIS. The iso-$T_{\rm eff}$ lines are slightly different with respect to figures 2 - 5, because of the different spectral response of the *ASCA* SIS.

et al. (1978). All the consequences described above have been sometimes considered as self-evident. For this reason, in the following we briefly revisit the basic equations of the hydrostatic loop model, with a formulation slightly different from the one usually known (see e.g. Bray et al. 1991).

For loops below the pressure scale height, the plasma pressure is practically constant along the loop, and the energy balance equation

$$E_{\rm H} - n_{\rm e}^2 P(T) = {\rm div} F_{\rm c} \ , \tag{9}$$

where $E_{\rm H}$ is the heating term, $n_{\rm e}$ the plasma electron pressure, $P(T)$ the plasma emissivity, and $F_{\rm c}$ the heat flux, can be rewritten in *adimensional form.* Taking advantage of the equation of state, the Spitzer formulation of the heat flux, and the RTV scaling laws (Eq. (1) and (2)), this equation can be expressed in terms of loop length and peak temperature as:

$$\alpha \ \frac{T_{\rm max}^{7/2}}{L^2} \ + \ \beta \ \frac{T_{\rm max}^6 P(T)}{T^2 L^2} \ = \ \gamma \frac{{\rm d}^2 T^{7/2}}{{\rm d}s^2} \ , \tag{10}$$

where α, β, and γ are numerical constants, and s is the field line coordinate along the loop. In the range $10^{5.1} < T < 10^7$ K, i.e. in the region of interest from the point of view of the X-ray emission and largely dominant (Bray et al. 1991), the radiative loss function can be approximated as $P(T) \sim T^{-1/2}$ (Rosner et al. 1978), and the above equation takes the form:

$$\kappa_1 + \kappa_2 T'^{-5/2} \ = \ \frac{{\rm d}^2 T'^{7/2}}{{\rm d}s'^2} \ , \tag{11}$$

where κ_1 and κ_2 are new constants, $T' = T/T_{\rm max}$, and $s' = s/L$. Therefore, the solution is invariant for a change of the spatial scale and of the temperature scale. In a similar way, the differential emission measure

$$DEM(T) = \frac{n_e^2}{\mathrm{d}T/\mathrm{d}s} , \quad (12)$$

using the RTV scaling law (Eq. (1)) and the plasma state equation, can be expressed as a function of the same adimensional variables, T' and s':

$$DEM(T') = \kappa_3 \frac{p}{T'^2 \mathrm{d}T'/\mathrm{d}s'} \quad (13)$$

The above equation shows that the DEM shape vs. T' is fixed, as well as its temperature range, because the choice pL fixes $T_{\rm max}$. In practice, once $T_{\rm max}$ (i.e. the product pL) has been chosen, the solution and the loop spectrum are completely determined. Different loops along the $pL \propto T_{\rm max} = constant$ locus then yield the same DEM shape, and hence the same spectrum; the DEM curves will be higher for higher pressure loops (while maintaining the same shape) as shown by the equation, but spatially unresolved observations could not distinguish higher pressures from larger covering factors. Hence, it is intrinsically impossible to constrain separately p and L, whatever the detector energy resolution or the counting statistics considered, if the pressure is uniform.

However, since our model loops are subject to gravity, this invariance is broken. We can expect that an instrument sensitive enough and/or with spectral resolution high enough, might be able to discriminate somehow among these models, i.e. to reduce the size of the elongated confidence region. This might be the case discussed in Sect. 5.

Finally, note that for relatively low counting statistics ($\sim 10^3$ total counts or less), the input IPC and PSPC spectra may be fitted equally well, in some cases (Fig. 2 and 4), by another class of models with (a) extension above the pressure scale height, (b) almost the same, relatively low base pressure, and (c) semi-length unconstrained at the high values. This can be explained by two effects: the limited sensitivity of the detectors to high temperature plasma components, whose emission falls outside the instrument energy band, and the limited amount of high temperature plasma near the loop top in the fitting models. In other words, since in the grid models the bulk of the emission comes from the loop region below the pressure scale height and the emission of plasma at temperatures above $\sim few \times 10^7$ K peaks where the instrument effective area is substantially reduced, any of these low-p_0, high-L, high-$T_{\rm max}$ grid models produces almost the same spectrum as seen from the IPC or the PSPC. Some improvement in discriminating these models is possible only with detectors with a wider energy band pass on the high energy side, such as the *ASCA* SIS (see Sect. 5.2).

(b) Input models with $H \geq s_{\rm p}$

For the input loops rising near or above the pressure scale height, the simulations indicate that, with a number of counts between 10^3 and 10^4, we tend to get closed confidence regions, i.e. the spectral fitting allows to constrain the loop parameters, and in particular the loop base pressure. This occurs only for input loops with $H \gtrsim s_{\rm p}$ because the emission measure distribution, and hence the shape of the emission spectrum, is no more determined solely by the value of $T_{\rm max}$, but also by the ratio $H/s_{\rm p}$. In Fig. 7 we plot, for each input loop, the function $T \times DEM(T)$ which, multiplied by the instrument-folded emissivity function $G(j,T)$, and integrated in $\mathrm{d}(\log T)$ yields the observed spectrum. Note the differences in shape and, in particular, the bending near the peak temperature for the loop models with large semi-length and relatively low base pressures. This bending is due to the relative lack of high temperature plasma. In the same figure we have also indicated the temperature ranges where most of the integrated plasma emission originates, as observed from each of the instruments here considered. These ranges correspond to the loop region from which 75% of the total emission originates, they are centered on the value, T_{50}, at which the volume-integrated emission reaches 50% of the total, and the ordinate indicates the $T \times DEM(T)$ value which would be derived from the integrated emission by evaluating the function $G(T)$ (Eq. (6)) at the value T_{50} and assuming the DEM constant over the above temperature range.

Note that some uncertainty on the determination of the loop semi-length, and hence on the maximum temperature, may still be present for the reasons explained above: for fixed base pressure, a larger loop height does not imply more emitting plasma if the pressure scale height has been exceeded. Hence, the spectral shape does not change substantially, and the fitting is unable to constrain the loop semi-length equally well as the base pressure.

(c) High-pressure Input models with $H \gg R_*$

In the case of input loops with relatively large base pressure (e.g. $p_0 \sim 25$ dyne cm^{-2}) and large semi-lengths ($L \geq 3 \times 10^{11} \approx 4R_*$), the confidence regions are again extended along the iso-$T_{\rm eff}$ lines, similarly to the loops below the pressure scale height considered above. This behavior appears to be in contradiction with our previous statement that the approach is able to constrain loops with $H \geq s_{\rm p}$. The reason is that, for these loops, $s_{\rm p}$ fails to describe the pressure distribution: the decrease of gravity with height allows a substantial fraction of plasma to be present near the loop top, and this plasma is at a relatively high temperature. In other words, the density decrease with height is limited by the local increase of the pressure scale height. This effect is visible in Fig. 7, by noting that the bending and the hump of the differential emission measure for the larger loops is less and less evident for larger and larger base pressure and semi-length (cases i – m). This behavior is confirmed by inspection of

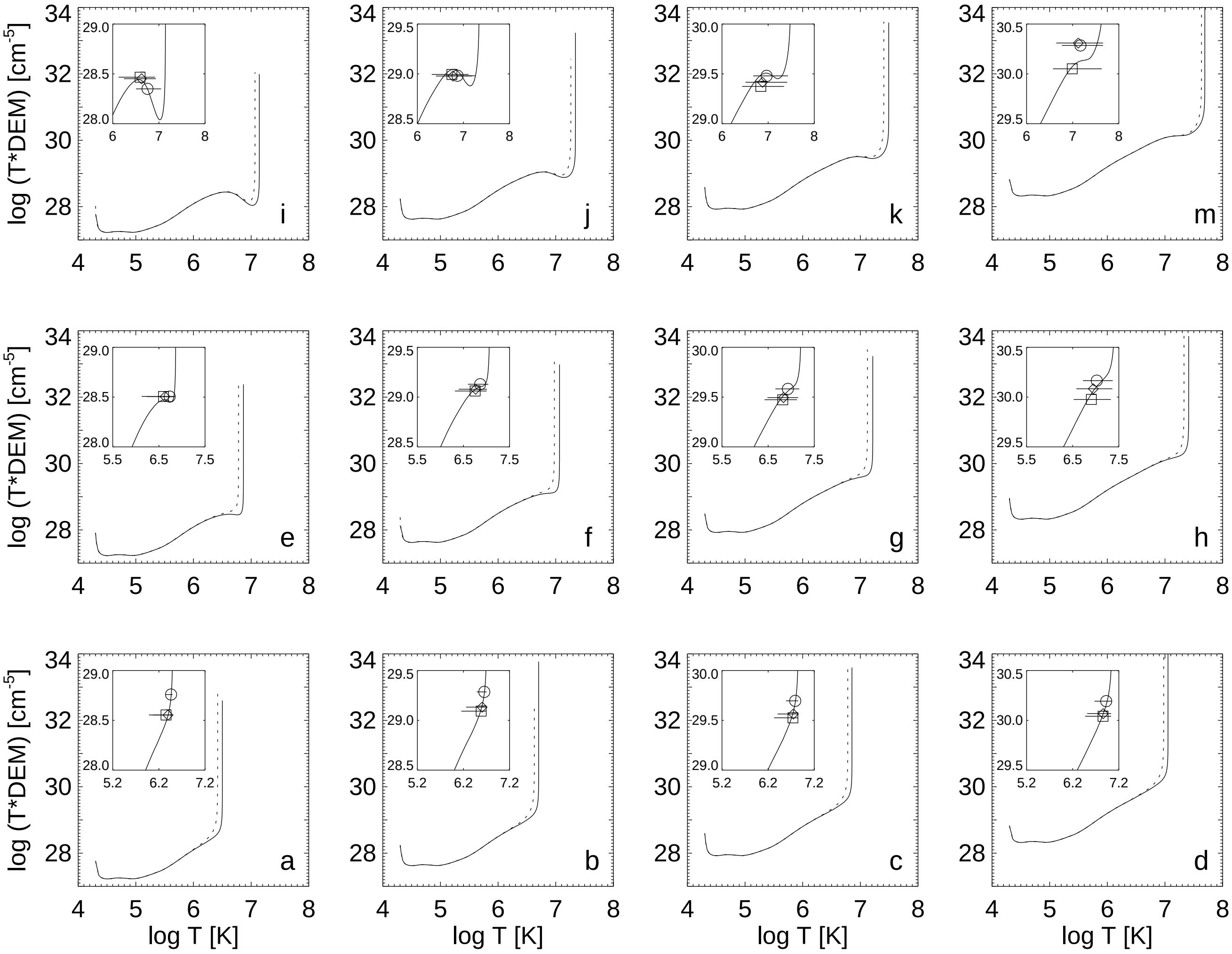

Fig. 7. Differential emission measure multiplied by the plasma temperature, $T \times DEM(T) = Tn_e^2/\nabla T$, as a function of the temperature for the input loop models considered. The three horizontal segments, in the enlarged portion of each plot shown in the inserts, span the temperature ranges over which 75% of the total emission originates, for the three instrument considered. The different symbols (diamonds for the *Einstein Observatory* IPC, squares for the *ROSAT* PSPC, and circles for the *ASCA* SIS) are located at the temperature, T_{50}, i.e. at which the volume-integrated emission along the loop reaches 50% of the total, and the ordinates correspond to the $T \times DEM$ values derived from the total emission if the emission measure were constant over the above temperature ranges. In each plot, the solid line curves refer to input loops with uniform heating per unit volume, while the dotted line curves have been obtained for an heating scale height equal to half the loop semi-length. In the latter cases, the peak temperature is systematically reduced by $\sim$ 20%.

the pressure fall along the loop, illustrated in Fig. 8: note that the pressure drops by about 20% in all the loops below the pressure scale height (cases a – d); for the largest loops (cases i – m) the drop changes from $\sim$ 80% (case i) to 60% (case m) as the base pressure (and the maximum temperature) increases. In the same figure, we show also the location, s_{90} along the loop where the spatially-integrated emission, in the 0.16-4 keV IPC energy band, reaches 90% of its total value. A smaller value of s_{90} means less emitting plasma near the loop top, and therefore less plasma at relatively high temperature. Note that the position s_{90} first tends to decrease for increasing loop semi-length (cases from a to i), and then increases again (cases i – m).

With the insight coming from Fig. 8, we have to reconsider the realism of the models with higher pressure and longer semi-length, because they still have a significant plasma pressure at the loop apex, where the magnetic field could be relatively weak, and it might be difficult to justify the assumption of magnetic confinement at large distance from the star's surface (up to 30 R_* for the case m). In addition, our assumption of uniform heating in the whole loop volume may be somehow arbitrary for such large values of L (see Sect. 5.3). Nevertheless, we have

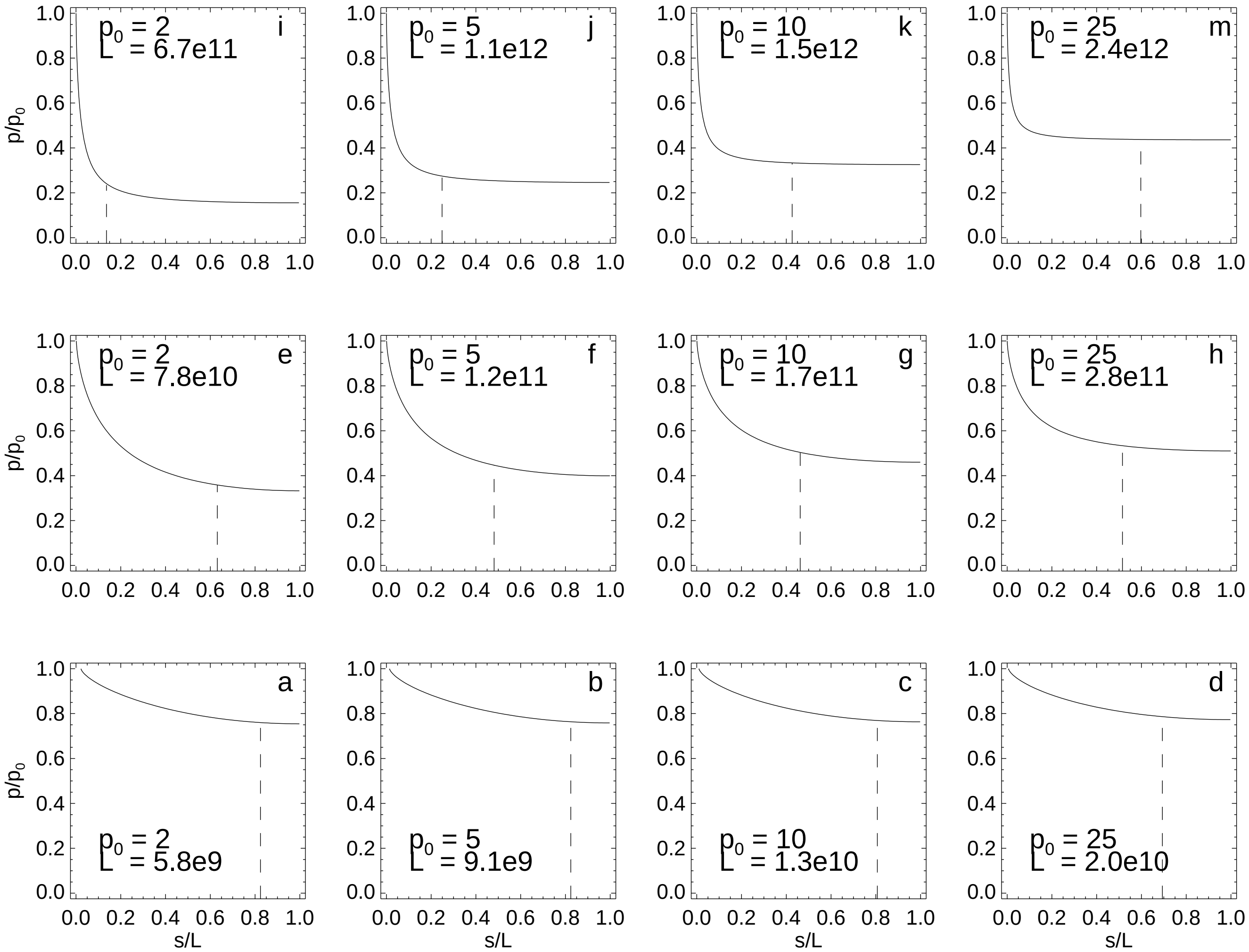

Fig. 8. Distribution of the plasma pressure, p, scaled by the base pressure, p_0, vs. s/L, i.e. the field line coordinate, s, scaled by the loop semi-length, L. The values of p_0 and L, in cgs units, are indicated in the legend of each panel. The 12 panels are arranged in the same order as in figure 2 and subsequent ones. The dashed vertical lines marks the position where the spatially-integrated emission, in the 0.16-4 keV IPC energy band, reaches 90% of its total value. Note that while for the shortest loops (cases *a*-*d*) the fractional pressure drop is small and nearly the same, for the larger loops (cases *i*-*m*) the drop is less and less pronounced for increasing loop base pressure, due to the effect of gravity decline. The competing roles of local pressure scale height and gravity decline determine how much emission comes from the high-temperature plasma near the loop top.

presented such models in order to provide as exhaustive a scenario as possible.

5.2. Comparison of Results Obtained with Different Instruments

The characteristics of the confidence regions in the parameter space share some analogy among all the instruments considered, but the loop model parameters can be, to some extent, better and better constrained with the better and better spectral resolution of the instruments considered. Among other things, the better discrimination of plasma temperatures yields the same diagnostic power with lower counting statistics.

The *ASCA* SIS simulations indicate a particular improvement of our ability to constrain the loop model parameters, due to its better resolution and its sensitivity to harder photons. Thanks to these characteristics, the confidence regions for the input loops shorter than the pressure scale height ($H \simeq 0.2 s_{rmp}$) are narrower than with the other instruments, and they get less and less elongated as we go from relatively lower values of the base pressure (cases *a* and *b*) to relatively higher values (cases *c* and *d*). In fact, the related loops contain hotter and hotter plasmas, and the effect we describe simply reflect the increasing ability of the *ASCA* SIS to discriminate the departure from the strict scale invariance of the loop model equations (Sect. 5.1*a*) as we go to harder and harder loop spectra. In this respect, note that even for these short loops the pressure decrease from base to top is about 20% (Fig. 8).

The improvement in our ability to constrain the loop model parameters with the analysis of *ASCA* SIS spectra is especially evident for input loops with $H \geq s_{\rm p}$ (Sect. 5.1*b*). The simulations yield smaller confidence regions (cases from *e* to *j*), and in particular they indicate that we can achieve a lower uncertainty on the loop semi-length (or peak temperature, since the base pressure is well constrained) than with the other instruments. Again, this result is due to the higher spectral resolution and the energy bandpass wide enough to have sensitivity to plasma emission at $E \gtrsim 1$ keV. For the same reason, some improvement can be achieved also for the input loops with quite high base pressure and large height above the stellar surface (cases *k* and *m*).

5.3. Effect of Heating Scale Height

For the sake of completeness, we have also explored what effects would be introduced in the results of the spectral fitting if the plasma heating were not uniform but would decrease exponentially with height. To this end, we have computed the twelve input loop spectra, as observed by the *ASCA* SIS, with the assumption of an heating scale height $s_{\rm H} \simeq L/2$. Note that no solution of the hydrostatic loop model equations can be found for smaller values of $s_{\rm H}$, because the energy balance equation cannot be satisfied (Serio et al. 1981). Then, we have performed a set of simulations, one for each input loop, assuming for the fitting the usual grid models with uniform heating distribution.

In Fig. 7 we show how the emission measure distributions, in the case of finite heating scale height (dotted curves), compare with the case of uniform heating: the DEM distribution is not affected except that for a decrease of $T_{\rm max}$ by about 20%. This small difference is reflected in the results of the simulations: for observations with *ASCA* SIS, we can expect a small but sizable error in recovering the input loop parameters; in all cases, the confidence regions are systematically shifted toward lower-L, higher-p_0 values. For most of the input loops the input parameter values fall just outside the 90% confidence region, except for the larger loops (cases i - m).

5.4. Single-loop vs. multiple-loop approach

Following the analogy with the solar corona, the stellar X-ray emission likely originates from an ensemble of loops with different characteristics, ranging from the compact, high-pressure loops found in solar active regions, to the extended, low-pressure loops in large scale structures. From this point of view, a multiple-loop model fitting would be desirable, instead of the single-loop approach of our simulations. However, our simplified single-loop study is presently motivated by three reasons: (a) a single-loop model may actually yield an adequate description of the observed spectra, as confirmed by most of the studies performed on real data so far (Schmitt et al. 1985; Stern et al. 1986; Ottman 1993), probably because a single class of loops may dominate the disk-integrated stellar X-ray emission; in fact, we note that the whole loop emission level scales as the square of the plasma density, hence the high-pressure loops are much brighter than the low-pressure ones (see Paper I); (b) the observations might not yield an high enough photon statistics to grant multiple loop fitting; (c) the single-loop approach allows a clear characterization of the influence of the various physical effects in determining the observed spectra; this would have been much harder if more than a single loop had been considered.

Whether or not a single-loop model may yield a good description of spectra from stellar coronae is a question that should be ultimately answered by real observational data. If real data will ask for a multiple-loop model fitting, and such a modeling is warranted by the data quality, this approach will be certainly worth pursuing.

6. Summary and Conclusions

We have performed an extensive set of simulations of X-ray spectral fitting with coronal loop models, considering three instruments: the *Einstein Observatory* IPC, the *ROSAT* PSPC, and the *ASCA* SIS. The aim of these simulations has been to test the effectiveness and self-consistency of the loop modeling approach - the natural and physically motivated evolution of present day data fitting methods - and to find which constraints on the loop parameters could be derived from the analysis of real data.

We have assumed that the coronal X-ray emission is dominated by a single class of constant cross-section loops, and it originates from a plasma with fixed (cosmic) abundances.

The distribution of the "best-fit" values over the loop parameter space considered has shown, for different input loops, three possible classes of fitting solutions:

(a) For loops smaller than the pressure scale height, i.e. with almost uniform plasma pressure, the confidence regions in the $p_0 - L$ parameter space are elongated and extend approximately along lines of constant $T_{\rm max}$ (or equivalently $T_{\rm eff}$). We have shown that this is due to an almost exact scale invariance of the equations describing an hydrostatic, constant-pressure loop model. This implies little capability to constrain separately p and L, but only their product, i.e. $T_{\rm max}$ (or $T_{\rm eff}$) according to the RTV scaling laws. Probably with instruments of higher spectral resolution it might be possible to discriminate among these cases.

(b) For loops longer than the pressure scale height, the invariance does not hold any more, and the spectral fitting yields closed confidence regions which allow to constrain separately all the loop parameters, with different levels of discrimination depending on the counting statistics, the spectral resolution, and the energy band of the detector. This result can be understood noting that the shape of the differential emission measure vs. plasma temperature, in the region where the X-ray emission originates, is not determined only by $T_{\rm max}$, but also by the ratio $H/s_{\rm p}$. In particular, the X-ray spectra provide us with a good diagnostic of the limited amount of high-temperature plasma near the loop top.

(c) For relatively high-pressure loops ($p_0 \sim 25$ dyne cm^{-2} in the case shown) extending far above the star's surface, the decrease of gravity along the loop limits the drop of the plasma pressure, with the consequence of having again nearly uniform pressure loops, with substantial high-temperature emitting plasma near the loop top. For these rather extreme models the shape of the confidence region is similar to that found in the case (a) above, and hence a good discrimination is possible of the peak plasma temperature, and therefore of the product of the base pressure and loop semi-length, but not of their values separately.

We emphasize that our simulations indicate that the loop modeling approach, with the assumptions described above, allows us to recognize *in all the cases explored* if the emitting plasma rests below the pressure scale height or not, and in the latter case to constrain the loop parameters much better. In this respect, our simulations show that the break of the scale invariance of the loop model equations, the changing shape of the differential emission measure distribution, and the ability to constrain separately all the loop model parameters, are three different aspects of the same scenario.

Finally, we have tested that the above conclusions do not depend on the heating scale height, although a small error can be expected in recovering the input loop parameters if uniform heating is assumed in the fitting model.

In this work we have considered only the case of a solar-type star. For stars of different spectral type, we do not expect qualitative differences in the results: the spectral fitting solutions should depend on the relative play of the pressure scale height with the loop height.

We conclude that, already with *ROSAT* and *ASCA* , the loop modeling approach should be able to provide a powerful diagnostic of the thermal stratification of stellar coronae.

Acknowledgements. We acknowledge extensive discussion with S. Serio, and useful comments and criticism from our colleagues A. Ciaravella, F. Damiani, F. Favata, G. Micela, F. Reale, and S. Sciortino. The authors also acknowledge partial support from Ministero dell'Universitá e della Ricerca Scientifica e Tecnologica, and Gruppo Nazionale di Astronomia del Consiglio Nazionale delle Ricerche.

References

Avni Y., 1976, ApJ 210, 642

Ciaravella A., Peres G., & Serio S. 1994a, A&A, submitted (Paper I)

Dempsey R.G., Linsky J.L., Fleming T.A., & Schmitt J.H.M.M. 1993, ApJ, 413, 333

Gehrels N. 1986, ApJ, 303, 336

Gehrels N. & Williams E.D., 1993, ApJ, 418, L25

Giampapa M.S., Golub L., Peres G., Serio S., & Vaiana G.S., 1985, ApJ, 289, 203

Harnden F.R., Fabricant D.G., Harris D.E., & Schwartz J. 1984, Smithsonian Obs. Spec. Rept. No. 393.

Kashyap, V., Rosner, R., Harnden, F.R., Jr., Maggio, A., Micela, G., & Sciortino, S. 1994, ApJ, 431, 402.

Maggio, A., Reale, F., Peres, G., & Ciaravella, A. 1994, CPC, 81, 105

Majer P., Schmitt J.H.M.M., Golub L., Harnden F.R., & Rosner R. 1986, ApJ, 300, 360

Morrison R., & McCammon D., 1983, ApJ, 270, 119

Ottmann R., 1993, A&A, 273, 546

Ottmann R., Schmitt J.H.M.M., & Kuerster M., 1993, ApJ, 413, 710

Pfeffermann E., et al. 1986, Proc. SPIE, 733, 519

Raymond, J.C., & Smith, B.W. 1977, ApJS, 35, 419

Raymond, J.C. 1989, private communication

Rosner, R., Tucker, W., & Vaiana G.S. 1978, ApJ, 220, 643

Rosner, R., Golub, W., & Vaiana G.S. 1985, ARAA, 23, 413

Schmitt, J.H.M.M., Harnden, F.R., Jr., Peres, G., Rosner, R., & Serio S. 1985, A&A, 288, 751

Schrijver C.J., Lemen J.R., & Mewe R., 1989, ApJ, 341, 484

Spitzer L., 1962, *Physics of Fully Ionized Gases*, (New York: Interscience), p. 143

Serio S., 1985, in "A Cosmic X-ray Spectroscopy Mission", ESA SP-239, p. 59

Stern R.A., Antiochos S.K., & Harnden F.R., 1986, ApJ, 305, 417

Tanaka Y., Inoue H., & Holt S.S., 1994, PASJ, 46, L37

Vaiana G.S., Rosner R., 1978, ARAA, 16, 393

Vesecky J.F., Antiochos S.K., & Underwood J.H., 1979, ApJ, 233, 987

Withbroe G.L. 1981, in "Solar Active Regions: a Monograph from Skylab Solar Workshop III", (Boulder: Colorado Ass. Univ. Press), p. 199

Wood B.E., Brown A., & Linsky J.L. 1995, ApJ, in press.

This article was processed by the author using Springer-Verlag LaTeX A&A style file *L-AA* version 3.